Electronic supplementary information for the paper:

Impact of the number of hydrogen bonds on proton conductivity in metallo-hydrogen-bonded organic frameworks: The more, the better at the maximum relative humidity

Shaoqiang Feng, [a] Fengxia Xie, [*a] Chengan Wan, [b] Feng Zhang, Lei Feng, [b] Chen Wen, [*b] and Xiaoqiang Liang [*a]

[a] *College of Environmental and Chemical Engineering, Xi'an Polytechnic University, Xi'an 710048, PR China. E-mail: anxiny@163.com, xq-liang@163.com*
[b] *Beijing Spacecrafts Manufacturing Factory, Beijing 100094, PR China. E-mail: 13552907280@163.com*
[c] *Key Laboratory of Photochemical Biomaterials and Energy Storage Materials, Heilongjiang Province and College of Chemistry and Chemical Engineering, Harbin Normal University, Harbin 150025, PR China.*

Table of Contents

I. Crystallographic data

Table S1 Selected bond lengths (Å) and angles (°) for **Ni-Ci-NH$_3$** and **Ni-Ci-H$_2$O**.

	Ni-Ci-NH$_3$		
Ni(1)−N(1)	2.141(3)	Ni(1)−N(1W)	2.1011(15)
Ni(1)−N(1a)	2.141(3)	Ni(1)−N(1Wa)	2.1011(15)
Ni(1)−N(1Wb)	2.1011(15)	Ni(1)−N(1Wc)	2.1011(15)
N(1)−Ni(1)−N(1W)	88.98(6)	N(1)−Ni(1)−N(1a)	180.00
N(1)−Ni(1)−N(1Wa)	91.02(6)	N(1)−Ni(1)−N(1Wb)	91.02(6)
N(1)−Ni(1)−N(1Wc)	88.98(6)	N(1W)−Ni(1)−N(1Wa)	86.11(6)
N(1W)−Ni(1)−N(1Wb)	180.00	N(1W)−Ni(1)−N(1Wc)	93.89(6)
N(1a)−Ni(1)−N(1Wa)	88.98(6)	N(1a)−Ni(1)−N(1Wb)	88.98(6)
N(1a)−Ni(1)−N(1Wc)	91.02(6)	N(1Wa)−Ni(1)−N(1Wb)	93.89(6)
N(1Wb)−Ni(1)−N(1Wc)	86.11(6)	N(1Wa)−Ni(1)−N(1Wc)	180.00
N(1a) −Ni(1)−N(1W)	107.0(2)		
	Ni-Ci-H$_2$O		
Ni(1)−O(1W)	2.076(4)	Ni(1)−O(2W)	2.077(3)
Ni(1)−N(2)	2.084(4)	Ni(1)−O(1Wa)	2.076(4)
Ni(1)−O(2Wa)	2.077(3)	Ni(1)−N(2a)	2.084(4)
O(1W)−Ni(1)−O(2W)	90.61(14)	O(1W)−Ni(1)−N(2)	90.28(14)
O(1W)−Ni(1)−O(2Wa)	89.39(14)	O(1W)−Ni(1)−N(2a)	89.72(14)
O(2W)−Ni(1)−N(2)	88.53(14)	O(1Wa)−Ni(1)−O(2W)	89.39(14)
O(2W)−Ni(1)−O(6a)	180.00	O(2W)−Ni(1)−N(2a)	91.47(14)
O(1Wa)−Ni(1)−N(2)	89.72(14)	O(2Wa)−Ni(1)−N(2)	91.47(14)
N(2)−Ni(1)−N(2a)	180.00	O(1Wa)−Ni(1)−O(2Wa)	90.61(14)
O(1Wa)−Ni(1)−N(2a)	90.28(14)	O(2Wa)−Ni(1)−N(2a)	88.53(14)

Symmetry codes: a) 1−*x*, 1−*y*, −*z*; b) 1−*x*, 1−*y*, −*z*; c) *x*, 1−*y*, *z* for **Ni-Ci-NH$_3$**; a) 1−*x*, 1−*y*, −*z* for **Ni-Ci-H$_2$O**.

Table S2 Hydrogen-bonding geometry parameters (Å, °) for **Ni-Ci-NH$_3$** and **Ni-Ci-H$_2$O**.

D−H···A	d(D−H)	d(H···A)	d(D···A)	∠(DHA)
		Ni-Ci-NH$_3$		
N(1W)−H(1W1)···O(2d)	0.9100	2.4600	3.082(2)	126.00
N(2)−H(2)···O(1e)	0.96(4)	1.89(4)	2.846(3)	169(4)
N(1W)−H(1W2)···O(1e)	0.9100	2.1100	2.962(2)	155.00
N(1W)−H(1W3)···O(2f)	0.9100	2.1600	3.044(2)	163.00
C(5)−H(5)···O(2)	0.9500	2.4800	2.801(3)	100.00
		Ni-Ci-H$_2$O		
N(1)−H(1)···O(1b)	0.8600	1.9500	2.763(6)	157.00
O(2W)−H(2WB)···O(2c)	0.8100	2.0700	2.750(5)	141.00
O(2W)−H(2WA)···O(1b)	0.8300	2.5800	3.169(5)	129.00
O(2W)−H(2WA)···O(2b)	0.8300	2.0300	2.838(5)	162.00
O(1W)−H(1WA)···O(2d)	0.9600	2.0000	2.802(5)	140.00
O(1W)−H(1WB)···O(1e)	0.9600	1.7400	2.688(5)	168.00

Symmetry codes: d) −1/2+*x*, 1/2+*y*, −1+*z*; e) *x, y,* −1+*z*; f) 3/2−*x*, 1/2+*y*, 1−*z* for **Ni-Ci-NH$_3$**; b) 1−*x*, 1/2+*y*, 1/2−*z*; c) 1/2−*x*, 1−*y*, −1/2+*z*; d) −1/2+*x*, *y*, 1/2−*z*; e) *x*, 1/2−*y*, −1/2+*z* for **Ni-Ci-H$_2$O**.

II. Characterization: PXRD patterns

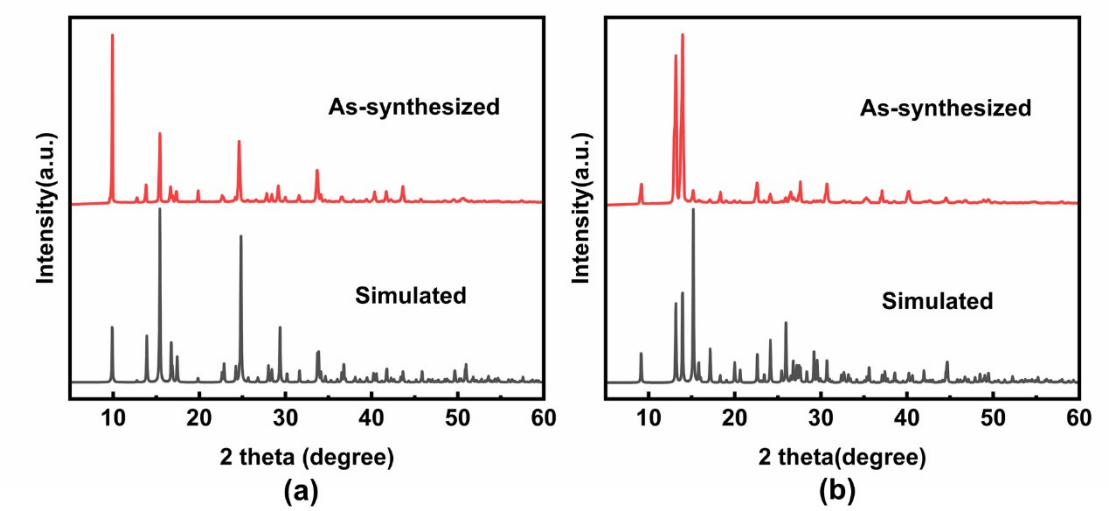

Fig. S1 The PXRD patterns for **Ni-Ci-NH_3** (a) and **Ni-Ci-H_2O** (b) of a simulation based on single-crystal analysis and as-synthesized bulk crystals.

III. Characterization: Infrared absorption spectra

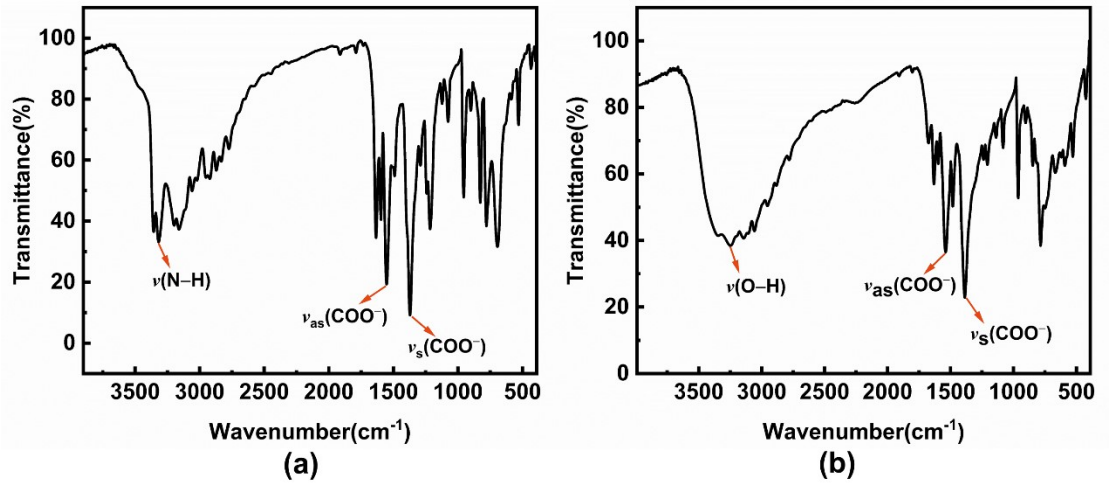

Fig. S2 IR absorption spectrum of **Ni-Ci-NH_3** (a) and **Ni-Ci-H_2O** (b) in the solid state at room temperature.

IV. Characterization: SEM images

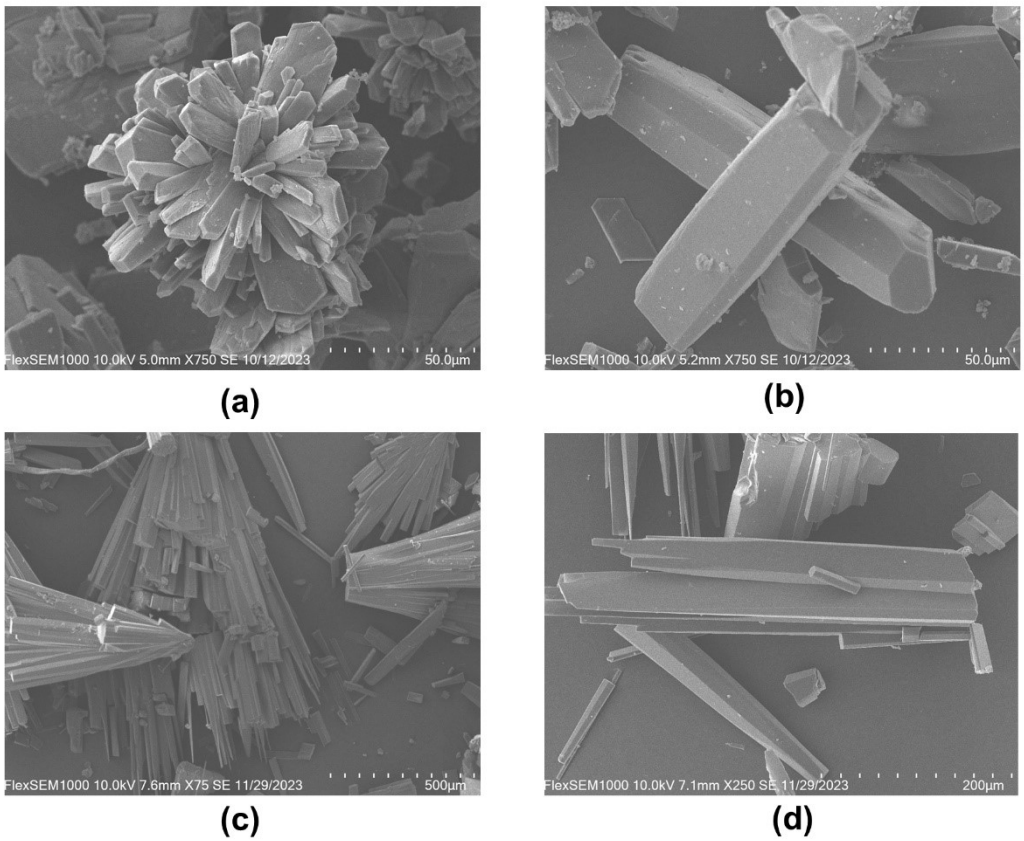

Fig. S3 SEM images of the full (a) and partial (b) views of **Ni-Ci-NH_3** as well as the full (c) and partial (d) views of **Ni-Ci-H_2O**.

V. Hydrophilicity: Water adsorption and water contact angle

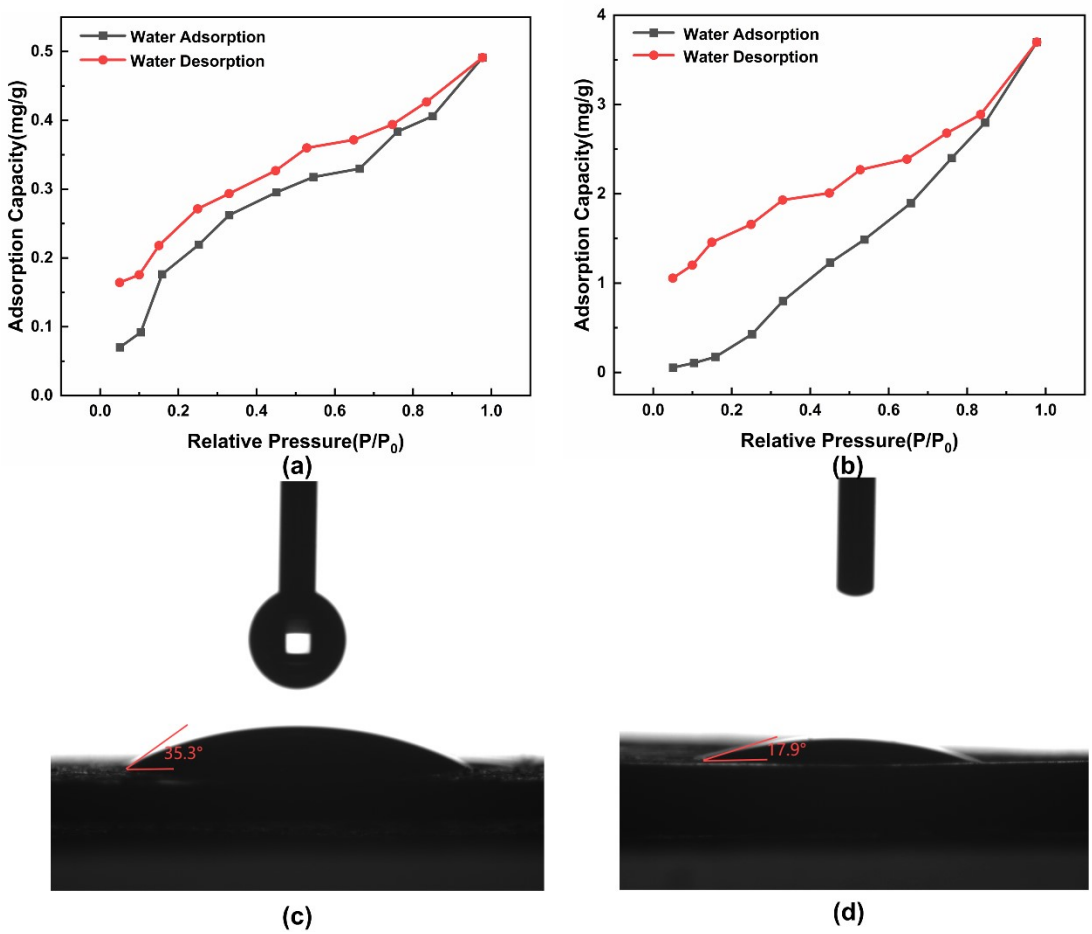

Fig. S4 Water adsorption−desorption isotherms for **Ni-Ci-NH_3** (a) and **Ni-Ci-H_2O** (b). Water contact angles of **Ni-Ci-NH_3** (c) and **Ni-Ci-H_2O** (d) at 298 K.

VI. Proton conduction

·Impedance spectra of powder samples

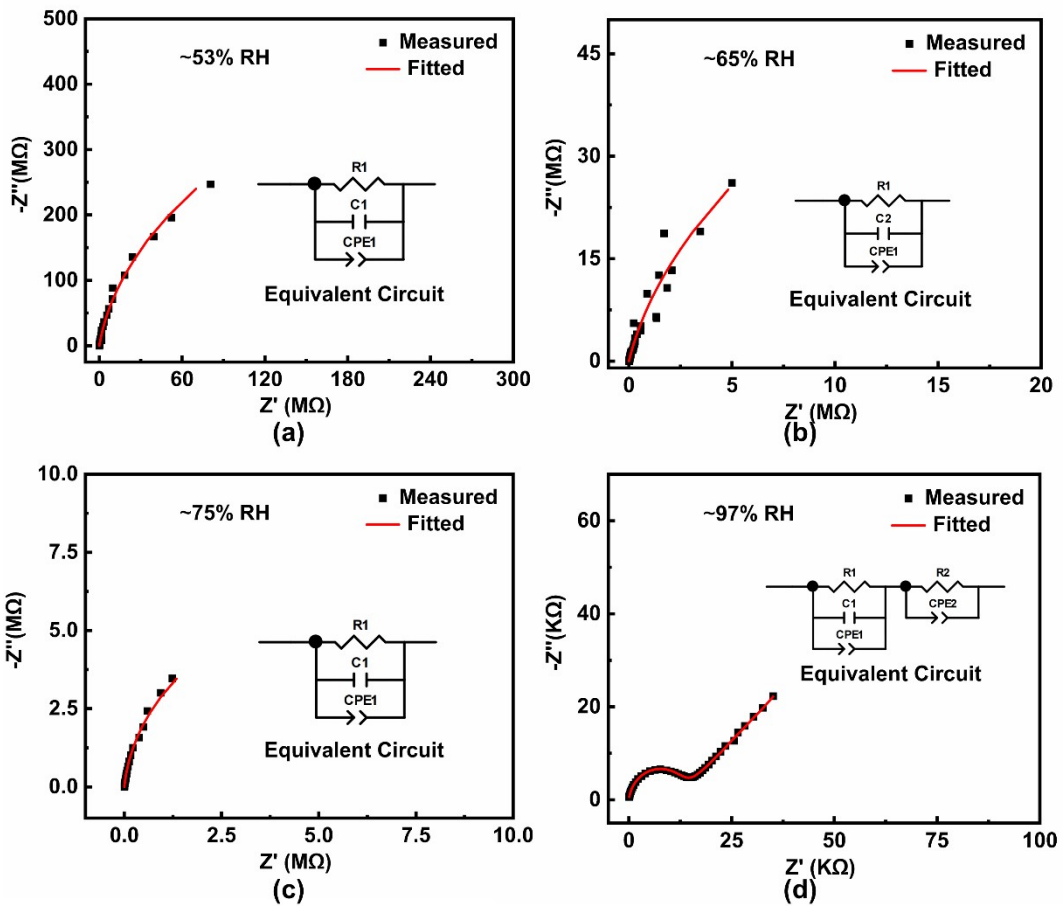

Fig. S5 Nyquist plots of **Ni-Ci-NH_3** at ~53% (a), ~65% (b), ~75% (c) and ~97% (d) RHs (relative humidities) and 298 K (R1, bulk resistor; R2, grain boundary resistor; CPE, constant phase element; C1 and C2 capacitor).

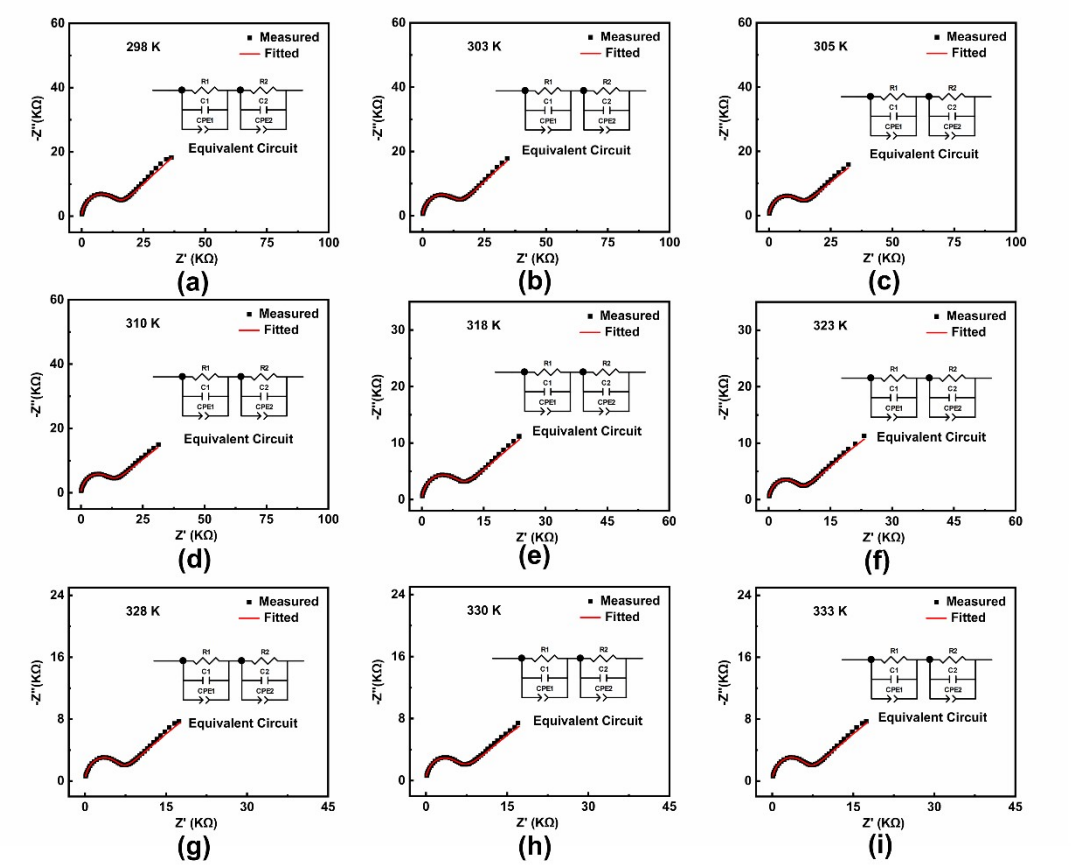

Fig. S6 Nyquist plots of **Ni-Ci-NH_3** at 298 K (a), 303 K (b), 305 K (c), 310 K (d), 318 K (e), 323 K (f), 328 K (g), 330 K (h) and 333 K (i) under ~97% RH (R1, bulk resistor; R2, grain boundary resistor; CPE1 and CPE2, constant phase element; C1 and C2, capacitor).

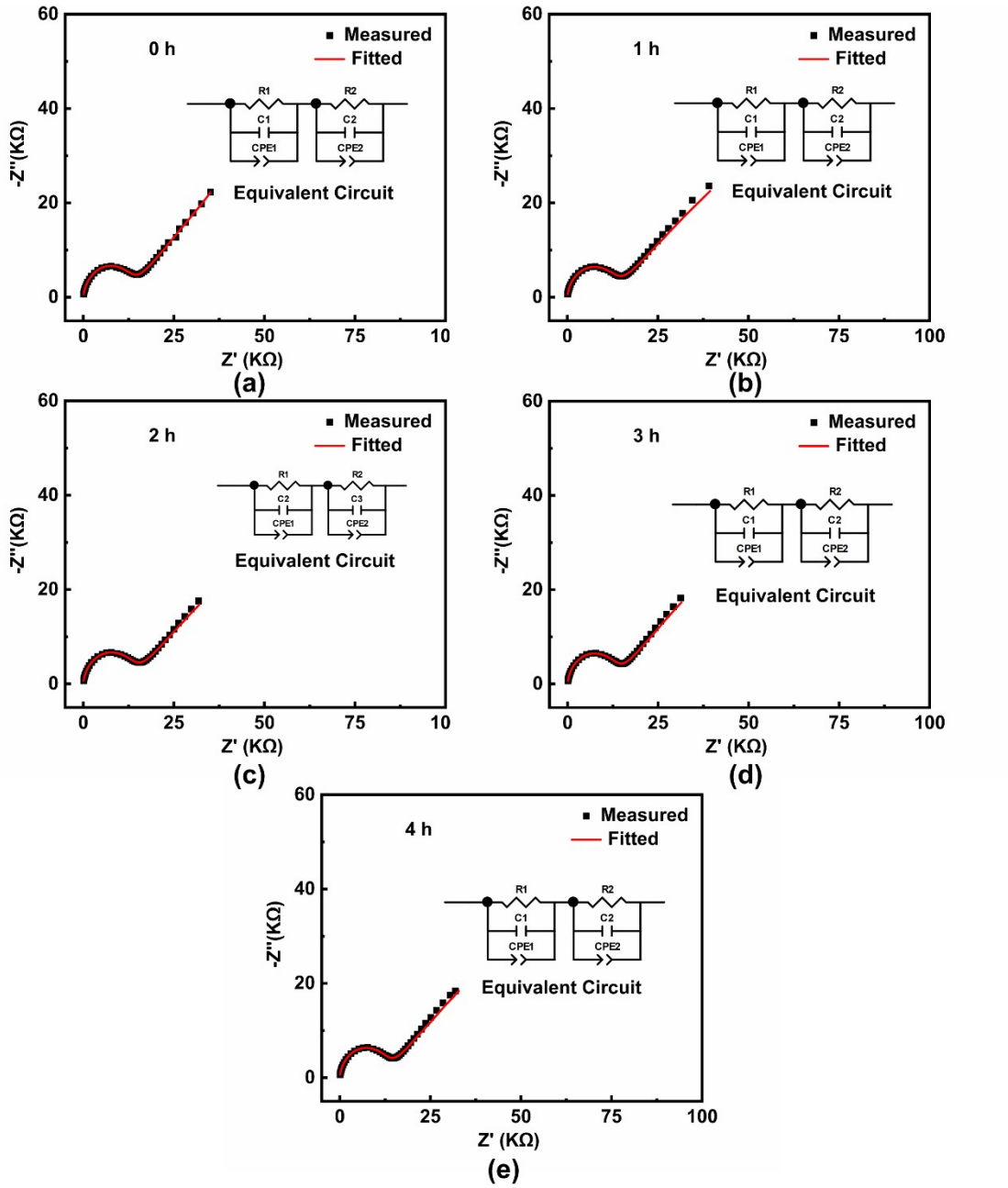

Fig. S7 Nyquist plots of **Ni-Ci-NH_3** at 0 h (a), 1 h (b), 2 h (c), 3 h (d) and 4 h (e) under 298 K and ~97% RH conditions (R1, bulk resistor; R2, grain boundary resistor; CPE1 and CPE2, constant phase element; C1 and C2, capacitor).

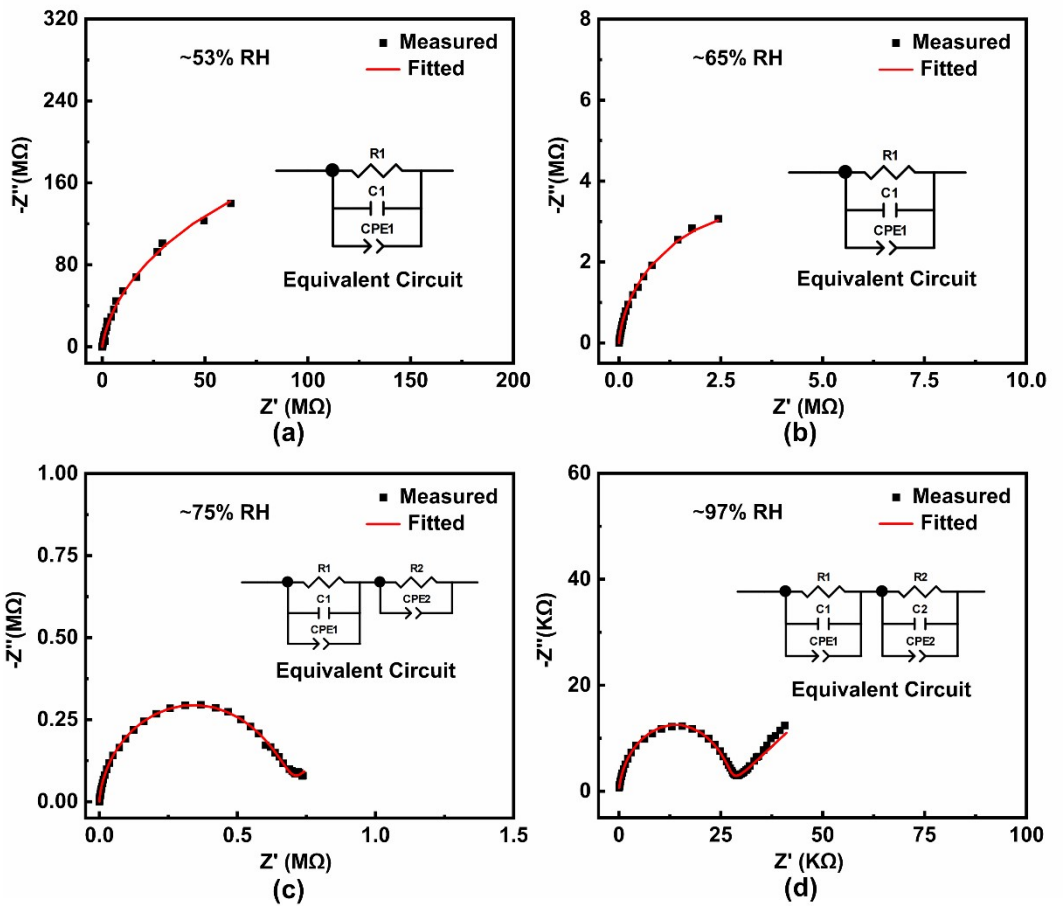

Fig. S8 Nyquist plots of **Ni-Ci-H_2O** at ~53% (a), ~65% (b), ~75% (c) and ~97% (d) RHs and 298 K (R1, bulk resistor; R2, grain boundary resistor; CPE1 and CPE2, constant phase element; C1 and C2 capacitor).

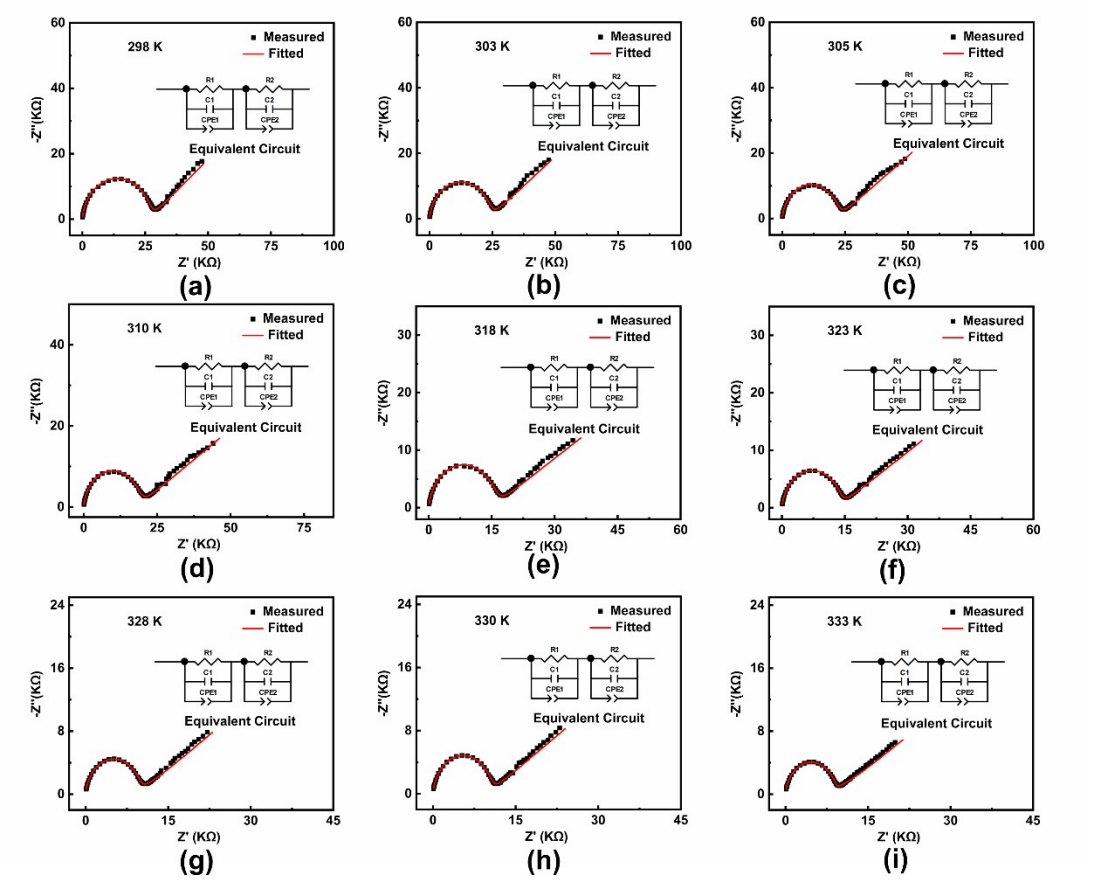

Fig. S9 Nyquist plots of **Ni-Ci-H_2O** at 298 K (a), 303 K (b), 305 K (c), 310 K (d), 318 K (e), 323 K (f), 328 K (g), 330 K (h) and 333 K (i) under ~97% RH (R1, bulk resistor; R2, grain boundary resistor; CPE1 and CPE2, constant phase element; C1 and C2, capacitor).

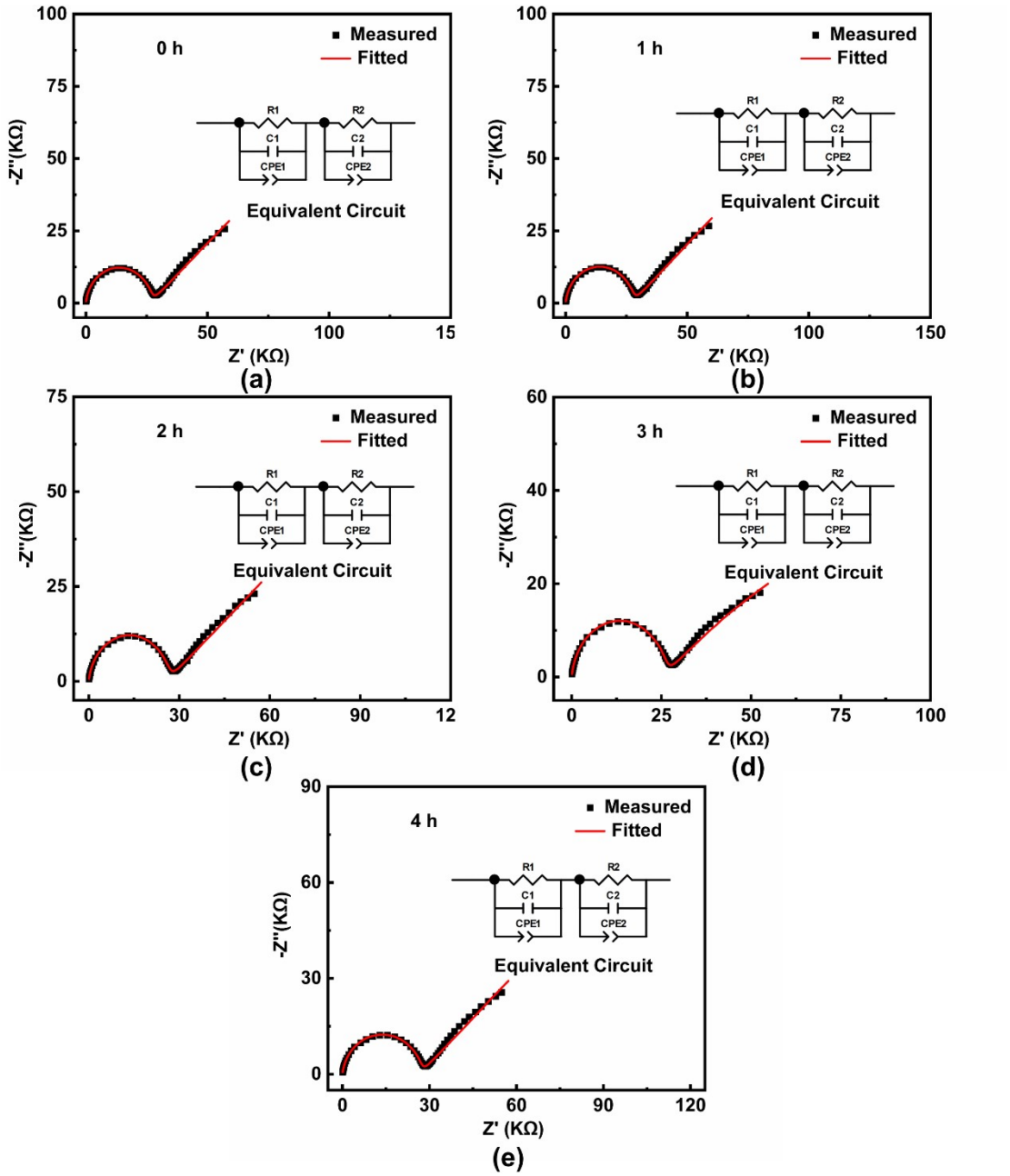

Fig. S10 Nyquist plots of **Ni-Ci-H_2O** at 0 h (a), 1 h (b), 2 h (c), 3 h (d) and 4 h(e) under 298 K and ~97% RH conditions (R1, bulk resistor; R2, grain boundary resistor; CPE1 and CPE2, constant phase element; C1 and C2, capacitor).

·**Determination of single crystal orientations**

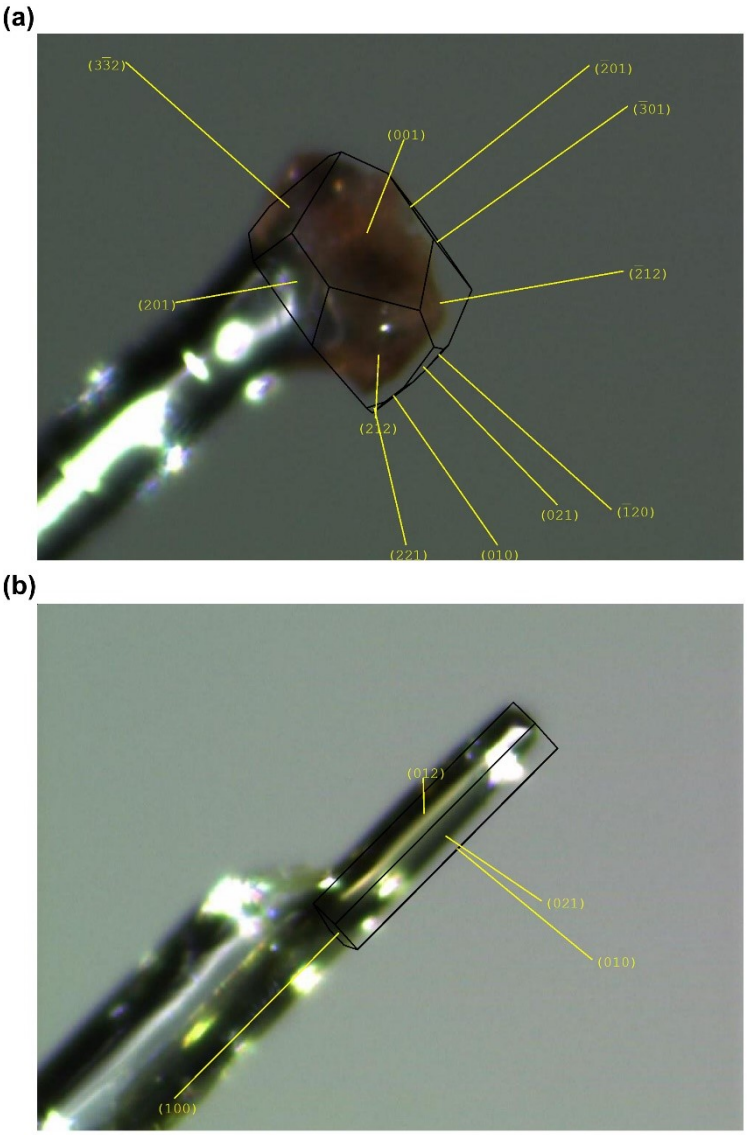

Fig. S11 The determined single crystal orientations of **Ni-Ci-NH_3** (a) and **Ni-Ci-H_2O** (b).

• **Determination of crystal size**

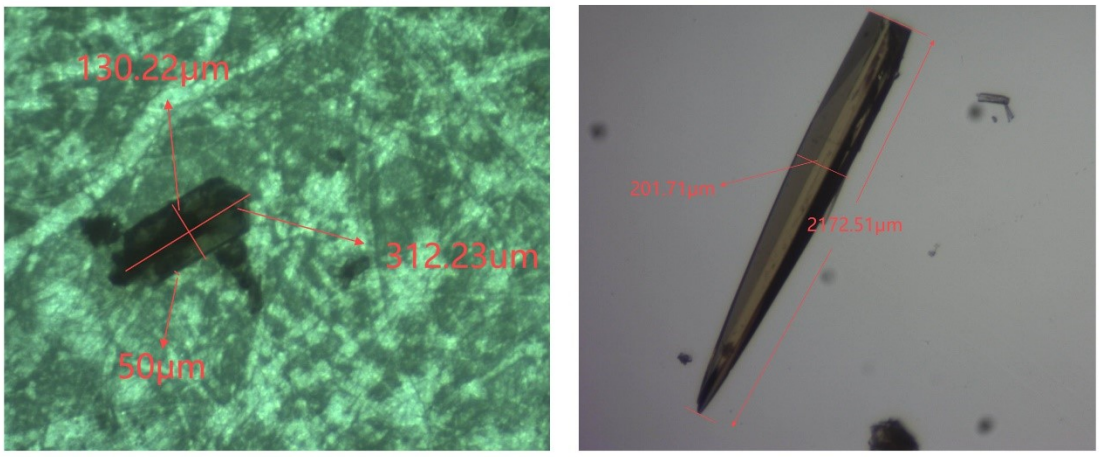

Fig. S12 The crystal size of **Ni-Ci-NH_3** (a) and **Ni-Ci-H_2O** (b) for single-crystal proton conduction.

· **Impedance spectra of single crystals**

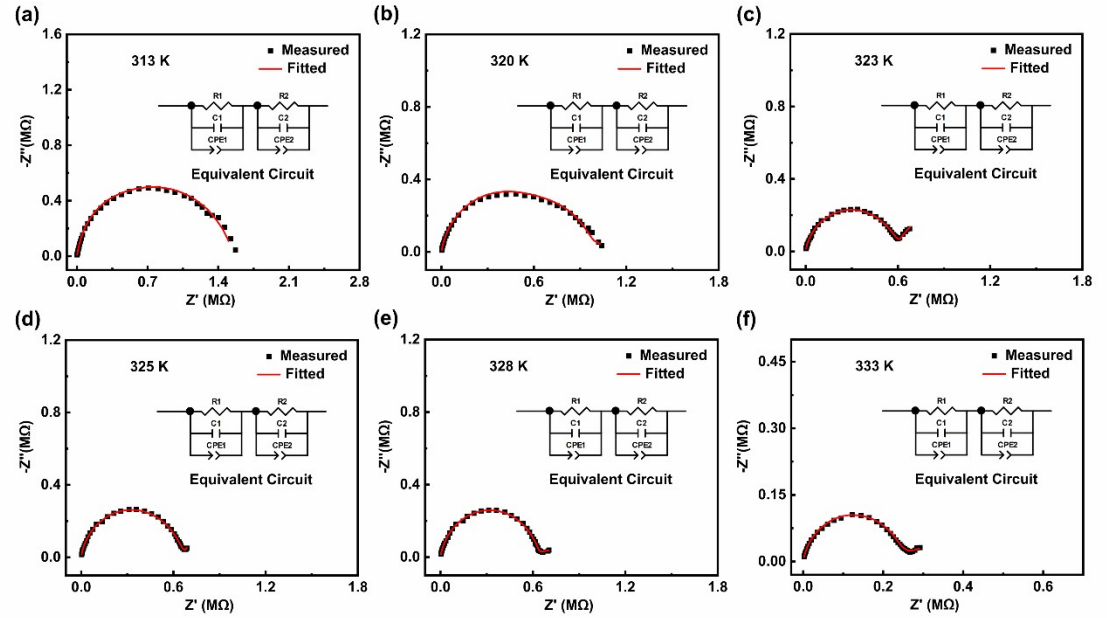

Fig. S13 Nyquist plots of **Ni-Ci-NH$_3$** along the [010] direction at 313 K (a), 320 K (b), 323 K (c), 325 K (d), 328 K (e) and 333 K (f) under ~97% RH (R1, bulk resistor; R2, grain boundary resistor; CPE1 and CPE2, constant phase element; C1 and C2, capacitor).

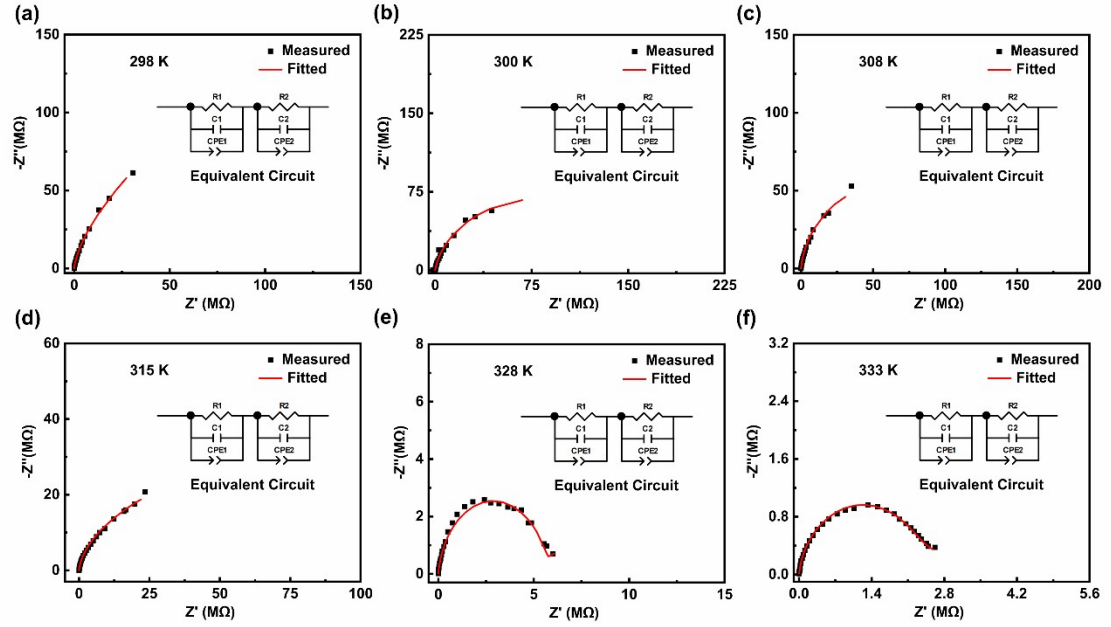

Fig. S14 Nyquist plots of **Ni-Ci-NH$_3$** along the [201] direction at 298 K (a), 300 K (b), 308 K (c), 315 K (d), 328 K (e) and 333 K (f) under ~97% RH (R1, bulk resistor; R2, grain boundary resistor; CPE1 and CPE2, constant phase element; C1 and C2, capacitor).

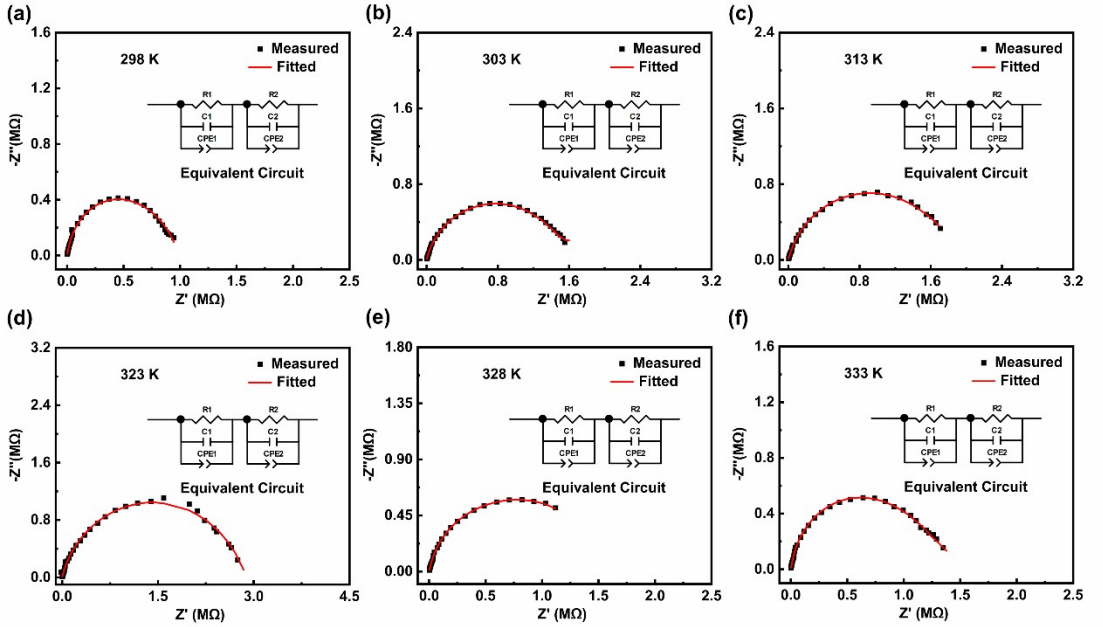

Fig. S15 Nyquist plots of **Ni-Ci-H_2O** along the [100] direction of at 298 K (a), 303 K (b), 313 K (c), 323 K (d), 328 K (e) and 333 K (f) under ~97% RH (R1, bulk resistor; R2, grain boundary resistor; CPE1 and CPE2, constant phase element; C1 and C2, capacitor).

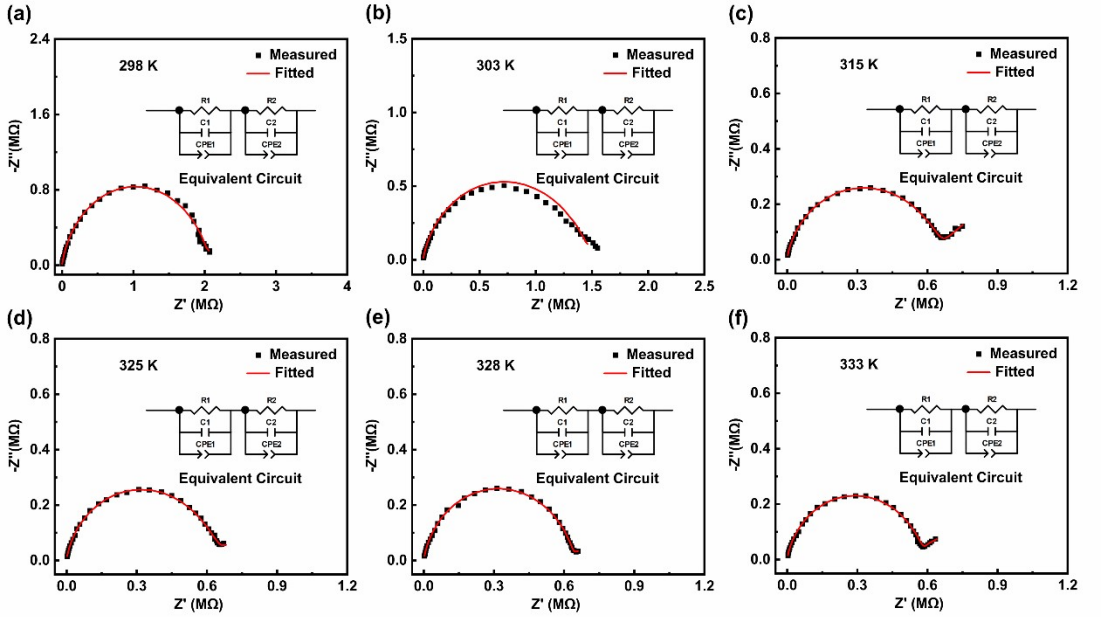

Fig. S16 Nyquist plots of **Ni-Ci-H_2O** along the [010] direction at 298 K (a), 303 K (b), 315 K (c), 325 K (d), 328 K (e) and 333 K (f) under ~97% RH (R1, bulk resistor; R2, grain boundary resistor; CPE1 and CPE2, constant phase element; C1 and C2, capacitor).

· **Single-crystal proton conduction**

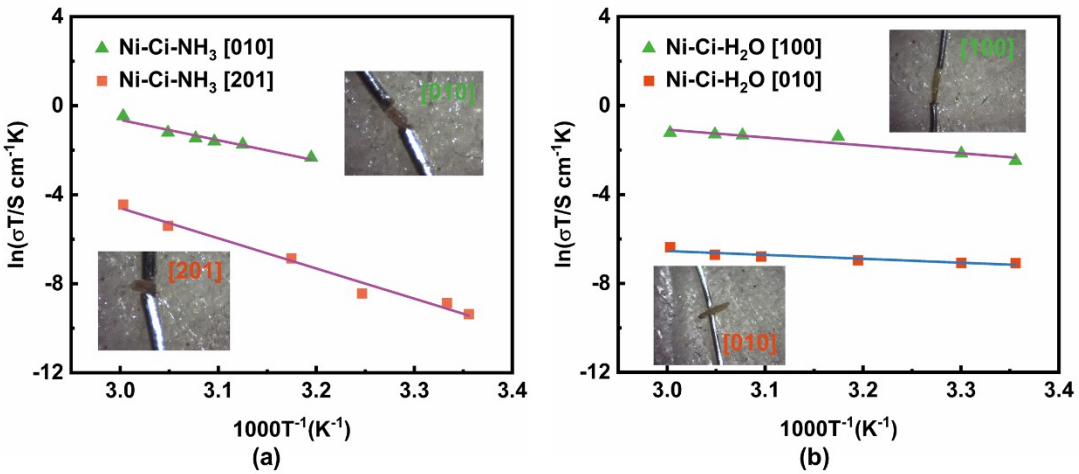

Fig. S17 Single-crystal proton conductivity of **Ni-Ci-NH$_3$** and **Ni-Ci-H$_2$O**. (a) Arrhenius plots of **Ni-Ci-NH$_3$** along the [010] and [201] directions at various temperatures under the ~97% RH condition. (b) Arrhenius plots of **Ni-Ci-H$_2$O** along the [100] and [010] directions at various temperatures under the ~97% RH condition.

Considering the temperature-dependent characteristic of single-crystal proton conductivity, we calculated the proton transfer activation energy (E_a) of Ni-Ci-NH$_3$ and Ni-Ci-H$_2$O along different directions at ~97% RH. Figure S13 shows the Arrhenius plots of ln(σT) versus 1000 T^{-1}, following a linear relationship. The obtained E_a values for Ni-Ci-NH$_3$ along the [010] and [201] direction are 0.790 eV and 1.171 eV, respectively, while the E_a values for Ni-Ci-H$_2$O along the [100] and [010] direction are smaller those of Ni-Ci-NH$_3$ along the [010] and [201] direction, which are 0.306 eV and 0.151 eV, respectively.

In theory, proton transfer along hydrogen-bonded networks should exhibit a lower activation energy, obeying the Grotthuss mechanism (0.1–0.4 eV). However, the above results deviate significantly from the theory. For example, the [010] direction of Ni-Ci-NH$_3$ is the extension of its hydrogen bonds, thus the proton conduction along the direction should follow the Grotthuss mechanism and the corresponding E_a value should fall in the range of 0.1–0.4 eV. However, the E_a value is far larger than 0.4 eV. Additionally, for Ni-Ci-H$_2$O, its hydrogen-bonded networks are along the [100] direction, thereby harvesting a lower E_a. However, its E_a value is higher that along the [201] direction. Notably, some phenomena similar to the above results were observed in water-mediated single-crystal proton conduction of other MOF materials, which are

summarized in Table S3.

Why was the phenomenon observed in water-mediated single-crystal proton conduction? It may be related with anisotropic hydrophilicity in single crystals. For single crystals, the main feature is the presence of anisotropy of physicochemical properties. As indicated by experimental results, the single-crystal proton conductivity shows an anisotropic behavior. Similarly, hydrophilicity as a kind of physicochemical property should display an anisotropy of single crystal. In fact, there is indeed the anisotropic hydrophilicity in single crystals, which were confirmed by hydrophilic measurements of some big single crystals.[1–4] Additionally, considering that the measured proton conductivity of MOFs and HMOFs under the low temperature is the water-mediated or water-assistant single-crystal proton conduction, thus besides effective hydrogen-bonded networks, another factor, i.e. hydrophilicity, has a contribution to activation energy, which cannot be ignored. Generally, a good hydrophilicity is conducive to proton migration/transfer with a lower barrier, and vice versa. However, anisotropic hydrophilicity is often overlooked due to the smaller size of MOF and HMOF materials. Thus, there is a larger deviation between the theoretic and experimental E_a values. For powder samples, anisotropic hydrophilicity was weakened or eliminated due to the random orientation leading to averaging effect, and effective hydrogen-bonded networks is predominated in proton conduction process. Consequently, the E_a show a good agreement between the experiment and the theory.

Table S3 Summarization of single-crystal proton conductivity and activation energy of **Ni-Ci-NH_3** and **Ni-Ci-H_2O** along with some reported proton conductors.

Materials	Crystalline facet	σ (S/cm)	E_a (eV)	T (K)	RH (%)	Reference
Ni-Ci-NH_3	[010]	1.88×10^{-3}	0.790	333	97	This work
	[201]	3.52×10^{-5}	1.171	333	97	This work
Ni-Ci-H_2O	[100]	8.84×10^{-4}	0.306	333	97	This work
	[010]	5.11×10^{-6}	0.151	333	97	This work
CoCa·$4H_2O$	[010]	1.00×10^{-3}	0.90	298	95	5
	[202]	4.49×10^{-6}	0.86	298	95	
	[20−1]	4.35×10^{-8}	0.58	298	95	
CFA-17	[011]	2.1×10^{-3}	~0.68	295	95	6
	[100]	2.1×10^{-5}	–	295	95	
NNU-6	[100]	1.92×10^{-2}	0.86	323	98	7
	[010]	2.42×10^{-4}	0.75	323	98	
	[001]	8.90×10^{-5}	0.53	323	98	
CuCo-orotate	[010]	$\sim 10^{-6}$	0.95	298	96	8
1·$3H_2O$	[100)	1.39×10^{-4}	0.48	303	95	9
	[010]	1.52×10^{-6}	0.56	303	95	

VII. Detail of hydrogen-bonded network

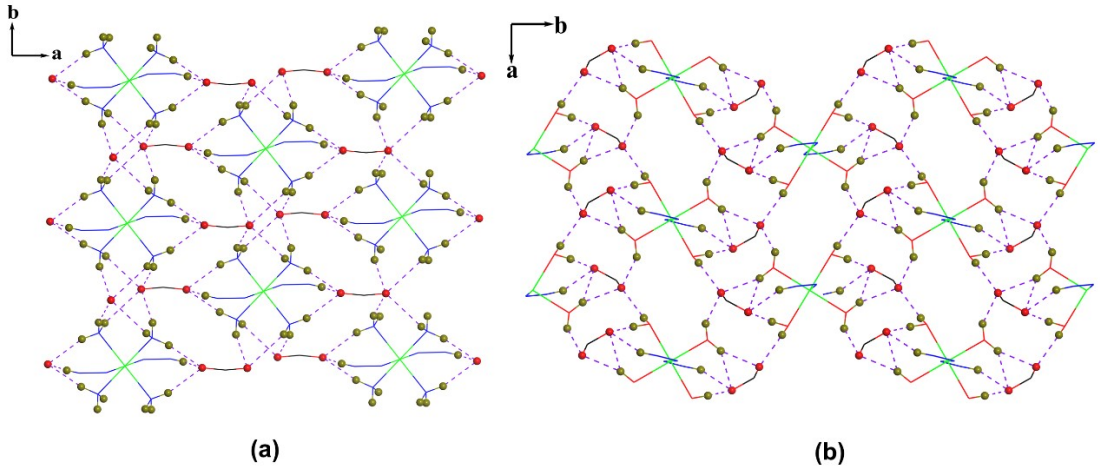

Fig. S18 Hydrogen-bonded networks of Ni-Ci-NH_3 (a) and Ni-Ci-H_2O (b). (Black, C; blue, N; red, O; cyan, Ni; dark green, H).

VIII. PXRD patterns after impedance measurements

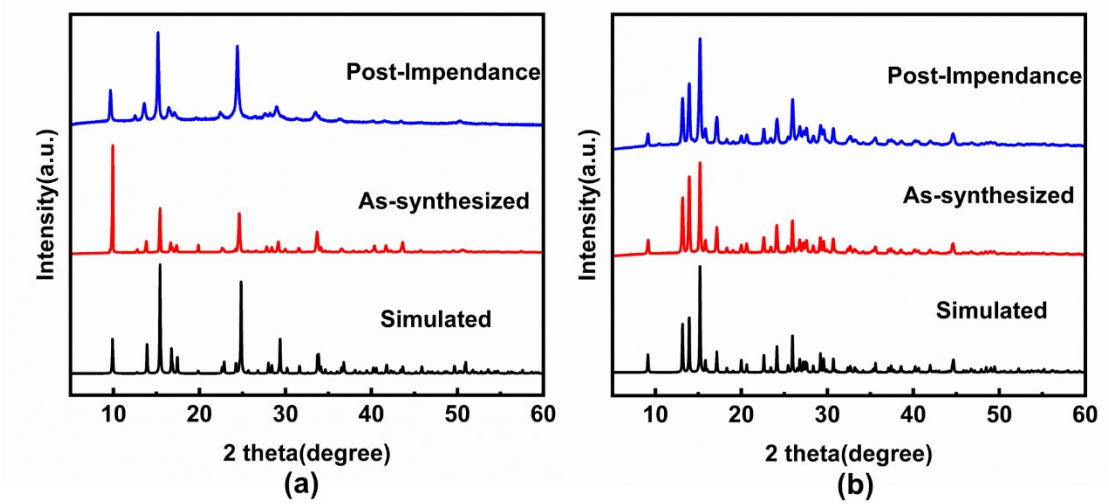

Fig. S19 PXRD patterns of simulations based on single-crystal analysis and after the impedance measurements for **Ni-Ci-NH_3** (a) and **Ni-Ci-H_2O** (b) (at ~97% RH and 298–323 K for 0–4 h).

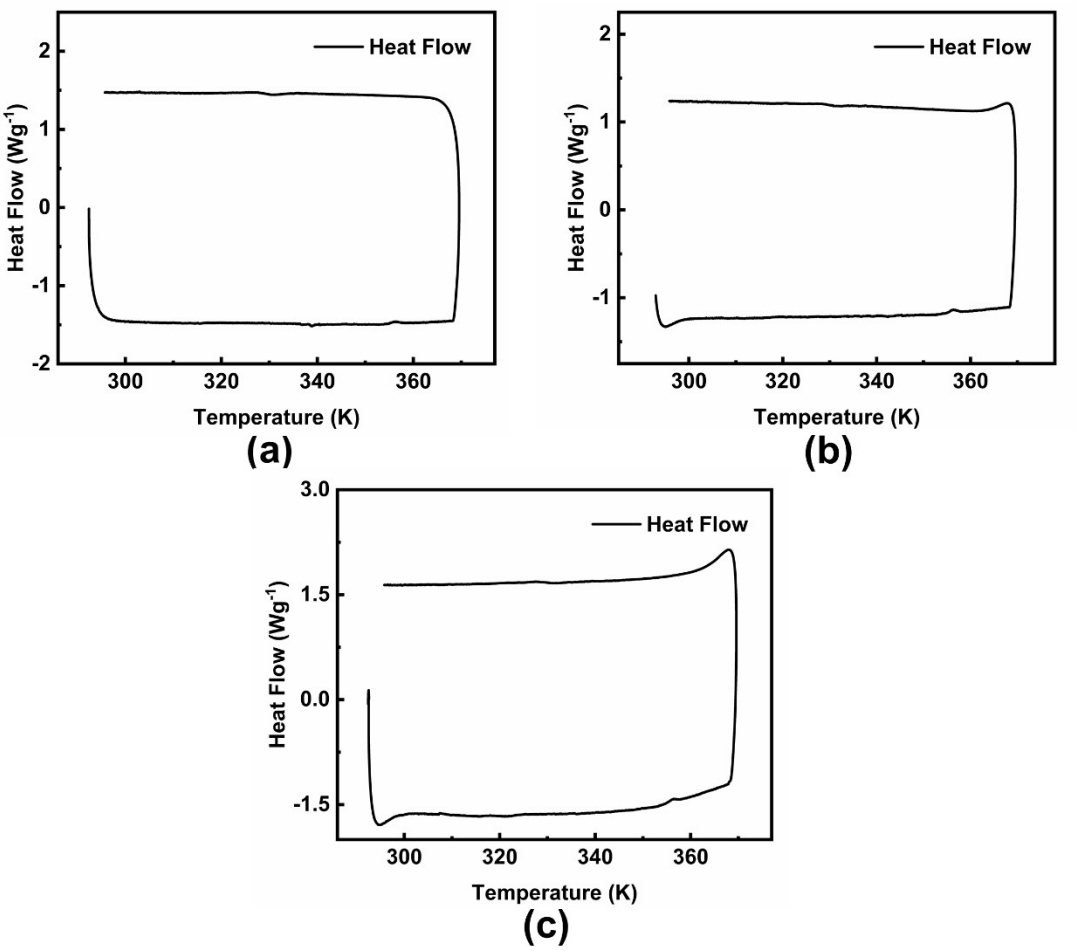

IX. Differential scanning calorimeter measurements

Fig. S20 Differential scanning calorimeter (DSC) curves of **Ni-Ci-NH_3** (a) and **Ni-Ci-H_2O** (b) and **blank sample** (c).

X. PXRD patterns after dielectric spectroscopy measurements

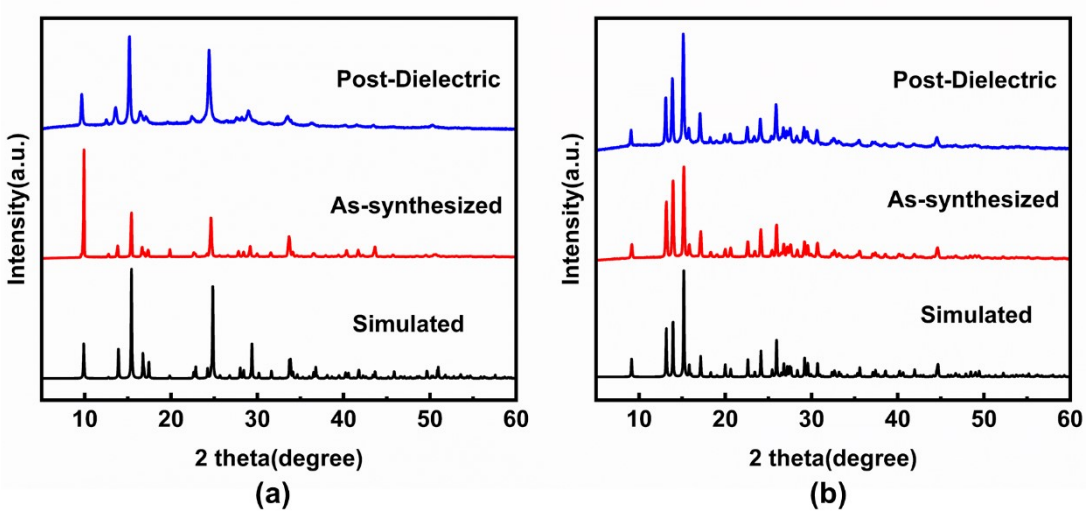

Fig. S21 PXRD patterns after dielectric spectroscopy measurements of **Ni-Ci-NH_3** (a) and **Ni-Ci-H_2O** (b).

XI. Comparison of chemical stability

Table S4 Comparison of chemical stability of **Ni-Ci-NH_3** and **Ni-Ci-H_2O** with reported MOF materials

Materials	pH range	Time (day or hour)	References
Ni-Ci-NH_3	2–12	3 d	This work
Ni-Ci-H_2O	2–12	3 d	This work
$[Me_2NH_2][Mn_2(L^1)(H_2O)_2]\cdot 2H_2O\cdot 2DMA$	4–8	24 h	10
USTC-8(In)	2–12	12 h	11
PCN-600(Fe)	2–11	24 h	12
FJI-H14 [a]	2–12	24 h	13
BUT-155 [b]	4–10	24 h	14
MIL-53(Al)	4–12	3 d	15
PCN-777	3–11	12 h	16
$[(CH_3)_2NH_2]_2[Eu_6(\mu_3\text{-}OH)_8(NDC)_6(H_2O)_6$ [c]	3.5–10	24 h	17
Co-2PPA [d]	3–11	12 h	18
Co-4PPA [d]	3–11	12 h	18

[a] $[Cu(BTTA)H_2O]_n\cdot 6nH_2O$; [b] Cu_4(tdhb); [c] NDC = naphthalenedicarboxylate; [d] HPPA = 4-(3-pyridinyl)-2-amino pyrimidine.

XII. Comparison of proton conductivity

Table S5 Comparison of proton conductivity of **Ni-Ci-NH_3** and **Ni-Ci-H_2O** with some reported proton conductors.

Materials	σ (S/cm)	E_a (eV)	T (K)	RH (%)	Reference
Ni-Ci-NH_3	6.22×10^{-4}	0.252	333	97	This work
Ni-Ci-H_2O	1.62×10^{-4}	0.298	333	97	This work
$LaRu(ox)_3 \cdot 10H_2O$	1×10^{-5}	0.32	298	95	19
$LaRu(ox)_3 \cdot 10H_2O$	3×10^{-8}	0.9	298	95	19
CPOS-4	7.40×10^{-4}	0.82	333	98	20
PCMOF-3 [e]	3.5×10^{-5}	0.17	298	98	21
$Fe(OH)(bdc\text{-}(COOH)_2)(H_2O)$	2.0×10^{-5}	0.21	298	98	22
$[Zn(L\text{-}LCl)(Cl)](H_2O)_2$	3.13×10^{-5}	0.34	299	98	23
$Gd_3(H_{0.75}O_3PCHOHCOO)_4 \cdot xH_2O$ (x = 15−16)	3.2×10^{-4}	0.23	294	98	24
Sr-SBBA [f]	4.4×10^{-5}	0.56	298	98	25
Ca-BTC-H_2O [g]	1.2×10^{-4}	0.18	298	98	26
$[Mo_5P_2O_{23}][Cu(phen)(H_2O)]_3 \cdot 5H_2O$ [h]	2.2×10^{-5}	0.232	301	98	27
$[H_3O][Mn_3\text{-}(\mu_3OH)(SDBA)_3(H_2O)](DMF)_5$ [i]	3×10^{-4}	0.93	307	98	28
MA-B-BDC [j]	4.32×10^{-4}	0.39	323	98	29
$[(CH_3)_2NH_2] \cdot [Zn_3Na_2(cpida)_3 \cdot 2.5DMF$ [k]	2.1×10^{-6}	0.81	368	97	30
$[LnL(H_2O)_3] \cdot 2H_2O$ [l]	1.6×10^{-5} (Eu) 1.33×10^{-5} (Dy)	0.91 0.87	348	97	31
Mg-BPTC	2.6×10^{-4}	1.18	373	98	32
Sr-BPTC [m]	2.7×10^{-4}	0.77	363	98	32
$K_2(H_2adp)[Zn_2(ox)_3] \cdot 3H_2O$ [n]	1.2×10^{-4}	0.45	298	98	33
In-IA-2D-2	4.2×10^{-4}	0.48	300	98	34
Cs-HPAA [o]	3.5×10^{-5}	0.40	297	98	35
$[Sm(H_5C_2P_2O_7)(H_2O)_2]$ ·Guest	3.4×10^{-5}	0.71	333	100	36
Fe-MOF	1.3×10^{-4}	0.385	333	98	37
MFM-500(Ni)	4.5×10^{-4}	0.43	298	98	38
Zn-pzdc-H_3O^+	2.42×10^{-3}	0.21	323	97	39
Mn-pzdc-H_3O^+	2.03×10^{-3}	0.10	323	97	39
Cu-Hpzdc-H_2O [p]	1.68×10^{-3}	0.35	323	97	39
JUC-125 [q]	1.5×10^{-4}	0.32	323	97	40
$\{[Pr_2Ca(betc)_2(H_2O)_7] \cdot H_2O\}_n$	3.2×10^{-5}	0.66	305	97	41
$[Pr(betc)(H_2O)_2]$	8.9×10^{-5}	0.33	313	97	41

$(H_2pip)_{0.5}\}_n$					
OCC 2 [r]	3.72×10^{-4}	0.21	299	97	42
LOF 1[s]	9.3×10^{-5}	0.33	303	97	43
PMOCP 3[t]	1.38×10^{-4}	0.14	323	97	44
$(H_{12}RCC1)^{12+}\cdot6(SO_4)^{2-}\cdot27.25(H_2O)$	6.10×10^{-5}	0.10	303	95	45
PPA	2.49×10^{-5}	0.27	325	97	46
[Cu(PPA)I]	1.64×10^{-4}	0.19	325	97	46
$[Co(PPA)_2(BDC)(H_2O)_2\cdot(PPA)_2(H_2BDC)_2(H_2O)]$ [u]	2.29×10^{-4}	0.24	325	97	46
[Ni $(PIP)_2(H_2O)_4]\cdot$NDS [v]	2.29×10^{-4}	0.58	353	98	47
$[DPBA\cdot PAM]_{0.5}\cdot0.2DMF\cdot H_2O$ [w]	1.54×10^{-5}	0.88	333	98	48
SCU-41[x]	1.7×10^{-4}	0.43	298	95	49
Co-2PPA	2.96×10^{-4}	0.29	333	97	18
Co-4PPA	2.78×10^{-5}	0.31	333	97	18

Note: σ = Proton conductivity; E_a = Activation energy; T = Temperature; RH = Relative humidity. [e] PCMOF-3 = $Zn_3(L)(H_2O)_2\cdot2H_2O$, L = $[1,3,5\text{-benzenetriphosphonate}]^{6-}$; [f] SBBA = 4,4′-sulfob-isbenzoic acid; [g] BTC = 1,3,5-benzenetricarboxylic acid; [h] Phen = phenanthroline; [i] H_2SDBA = 4,4′-sulfonyldibenzoic acid; [j] B-BDC = 5-borono-1,3-benzenedicarboxylic acid; [k] H_3cpida = (N-(4-carboxyphenyl)iminodiacetic acid; [l] L = N-phenyl-N′-phenylbicyclo-[2,2,2]-oct-7-ene-2,3,5,6-tetracarboxdiimide tetracarboxylic acid, Ln = Eu, Dy; [m] H_4BPTC = 2,2′,6,6′-tetracarboxybiphenyl; [n] H_2adp = adipic acid; ox = oxalate; [o] HPAA = R,S-hydroxyphos-phonoacetic acid; [p] H_2pzdc = 2,3-pyrazinedicar-boxylic acid. [q] JUC-125 = $\{[Gd_4(R\text{-ttpc})_2(R\text{-Httpc})_2(HCOO)_2(H_2O)_8]\cdot4H_2O\}_n$; [r] OCC 2 = $(H_3betc)_2(H_2\text{-Mepip})\cdot(H_2O)$; [s] LOF 1 = $\{[Er_3(pmpc)(C_2O_4)_3(H_2O)_7]\cdot2H_2O\}_n$; [t] PMOCP3 = $\{Cd(D\text{-}pmpcH)(H_2O)_2Cl_2\}_n$, D-$H_3$pmpc = 1-(phosphonomethyl)piperidine-3-carboxylic-acid; [u] $Co(PPA)_2(BDC)(H_2O)\cdot(PPA)_2(H_2BDC)_2(H_2O)$, H_2BDC = 1,4- benzenedicarboxylic acid); [v] NDS = 1,5-naphthalenedisulfonate; [W] DPBA = 3,5-diphosphonobenzoic acid, PAM = terephtalimidamide; [x] $(2\text{-Hmim})_2\cdot Ni(H_2PO_4)_4$(4,4′-bpy) (denoted SCU-41, 4,4′-bpy = 4,4′-bipyridine).

XIII. References

1 K. C. Pingali, T. Shinbrot, A. Cuitino, F. J. Muzzio, E. Garfunkel, Y. Lifshitz and A. B. Mann, AFM study of hydrophilicity on acetaminophen crystals, *Int. J. Pharm.*, 2012, **438**, 184–190.

2 M. Miyauchi, A. Shimai and Y. Tsuru, Photoinduced hydrophilicity of heteroepitaxially grown ZnO thin films, *J. Phys. Chem. B*., 2005, **109**, 13307–13311.

3 R. Kawamoto, S. Uchida and N. Mizuno, Amphiphilic guest sorption of $K_2[Cr_3O(OOCC_2H_5)_6(H_2O)_3]_2[\alpha\text{-}SiW_{12}O_{40}]$ ionic crystal, *J. Am. Chem. Soc.*, 2005, **127**, 10560–10567.

4 D. Kamiya and M. Horie, Hydrophilic and hydrophobic phenomena on silicon substrate for MEMS, *SPIE*, 1999, **3893**, 277–786X.

5 S. Bao, N. Li, J. M. Taylor, Y. Shen, H. Kitagawa and L. Zheng, Co–Ca phosphonate showing humidity-sensitive single crystal to single crystal structural transformation and tunable proton conduction properties, *Chem. Mater.*, 2015, **27**, 8116–8125.

6 H. Bunzen, A. Javed, D. Klawinski, A. Lamp, M. Grzywa, A. Kalytta-Mewes, M. Tiemann, H.A. K. von Nidda, T. Wagner and D. Volkmer, Anisotropic Water-Mediated Proton Conductivity in Large Iron(II) Metal–Organic Framework Single Crystals for Proton-Exchange Membrane Fuel Cells, *ACS Appl. Nano Mater.*, 2018, **2**, 291–298.

7 X. L. Cao, S. L. Xie, S. L. Li, L. Z. Dong, J. Liu, X. X. Liu, W. B. Wang, Z. M. Su, W. Guan and Y. Q. Lan, A Well-Established POM-based Single-Crystal Proton-Conducting Model Incorporating Multiple Weak Interactions, *Chem. Eur. J.Chemistry*., 2018, **24**, 2365–2369.

8 J. Stankiewicz, M. Tomás, I. T. Dobrinovitch, E. Forcén-Vázquez and L. R. Falvello, Proton Conduction in a Nonporous One Dimensional Coordination Polymer, *Chem. Mater.*, 2014, **26**, 5282–5287.

9 R. Li, S. Wang, X. Chen, J. Lu, Z. Fu, Y. Li, G. Xu, F. Zheng and G. Guo, Highly Anisotropic and Water Molecule-Dependent Proton Conductivity in a 2D Homochiral Copper(II) Metal–Organic Framework, *Chem. Mater.*, 2017, **29**, 2321–2331.

10 X. Chen, H. Jiang, B. Hou, W. Gong, Y. Liu and Y. Cui, Boosting chemical stability, catalytic activity, and enantioselectivity of metal–organic frameworks for batch and flow reactions, *J. Am. Chem. Soc.*, 2017, **139**, 13476–13482.

11 F. Leng, H. Liu, M. Ding, Q. P. Lin and H. L. Jiang, Boosting photocatalytic hydrogen production of porphyrinic MOFs: the metal location in metalloporphyrin matters, *ACS. Catal.*, 2018, **8**, 4583–4590.

12 K. Wang, D. Feng, T. F. Liu, J. Su, S. Yuan, Y. P. Chen, M. Bosch, X. Zou and H. C. Zhou, A series of highly stable mesoporous metalloporphyrin Fe-MOFs, *J. Am. Chem. Soc.*, 2014, **136**, 13983–13986.

13 L. Liang, C. Liu, F. Jiang, Q. Chen, L. Zhang, H. Xue, H. L. Jiang, J. Qian, D. Yuan

and M. Hong, Carbon dioxide capture and conversion by an acid-base resistant metal-organic framework, *Nat. Commun.*, 2017, **8**, 1233.

14 Y. Chen, B. Wang, X. Wang, L. H. Xie, J. Li, Y. Xie and J. R. Li, A copper(II)-paddlewheel metal–organic framework with exceptional hydrolytic stability and selective adsorption and aetection ability of aniline in water, *ACS. Appl. Mater. Interfaces.*, 2017, **9**, 27027−27035.

15 K. Leus, T. Bogaerts, J. De Decker, H. Depauw, K. Hendrickx, H. Vrielinck, V. Van Speybroeck and P. Van Der Voort, Systematic study of the chemical and hydrothermal stability of selected "stable" metal organic frameworks, *Micropor. Mesopor. Mater.*, 2016, **226**, 110–116.

16 D. Feng, K. Wang, J. Su, T. F. Liu, J. Park, Z. Wei, M. Bosch, A. Yakovenko, X. Zou and H. C. Zhou, A highly stable zeotype mesoporous zirconium metal–organic framework with ultralarge pores, *Angew. Chem., Int. Ed.*, 2015, **54**, 149–154.

17 D. X. Xue, Y. Belmabkhout, O. Shekhah, H. Jiang, K. Adil, A. J. Cairns and M. Eddaoudi, Tunable rare earth fcu-MOF platform: access to adsorption kinetics driven gas/vapor separations via pore size contraction, *J. Am. Chem. Soc.*, 2015, **137**, 5034–5040.

18 S. Wang, F. Xie, S. Zhang, X. Liang, Q. Gao, Y. Chen, F. Zhang, C. Wen, L. Feng and C. Wan, Water-assisted proton conduction regulated by hydrophilic groups in metallo-hydrogen-bonded organic frameworks: "like-attracts-like" between hydrophilic groups and water molecules, *CrystEngComm*, 2023, **25**, 4701–4715.

19 H. Okawa, M. Sadakiyo, K. Otsubo, K. Yoneda, T. Yamada, M. Ohba and H. Kitagawa, Proton conduction study on water confined in channel or layer networks of La(III)M(III)$(ox)_3$.$10H_2O$ (M = Cr, Co, Ru, La), *Inorg. Chem.*, 2015, **54**, 8529−8535.

20 G. Xing, T. Yan, S. Das, T. Ben and S. Qiu, Synthesis of Crystalline Porous Organic Salts with High Proton Conductivity, *Angew. Chem. Int. Ed.*, 2018, **57**, 5345-5349.

21 J. M. Taylor, R. K. Mah, I. L. Moudrakovski, C. I. Ratcliffe, R. Vaidhyanathan and G. K. Shimizu, Facile proton conduction via ordered water molecules in a phosphonate metal−organic framework, *J. Am. Chem. Soc.*, 2010, **132**, 14055–14057.

22 A. Shigematsu, T. Yamada and H. Kitagawa, Wide control of proton conductivity in porous coordination polymers, *J. Am. Chem. Soc.*, 2011, **133**, 2034–2036.

23 S. C. Sahoo, T. Kundu and R. Banerjee, Helical water chain mediated proton conductivity in homochiral metal–organic frameworks with unprecedented zeolitic unh-topology, *J. Am. Chem. Soc.*, 2011, **133**, 17950–17958.

24 R. M. P. Colodrero, K. E. Papathanasiou, N. Stavgianoudaki, P. Olivera-Pastor, E. R. Losilla, M. A. G. Aranda, L. León-Reina, J. Sanz, I. Sobrados, D. Choquesillo-Lazarte, J. M. García-Ruiz, P. Atienzar, F. Rey, K. D. Demadis and A. Cabeza, Multifunctional luminescent and proton-conducting lanthanide carboxyphosphonate open-Framework hybrids exhibiting crystalline-to-amorphous-to-crystalline transformations, *Chem. Mater.*, 2012, **24**, 3780–3792.

25 T. Kundu, S. C. Sahoo and R. Banerjee, Alkali earth metal (Ca, Sr, Ba) based

thermostable metal–organic frameworks (MOFs) for proton conduction, *Chem. Commun.*, 2012, **48**, 4998–5000.
26 A. Mallick, T. Kundu and R. Banerjee, Correlation between coordinated water content and proton conductivity in Ca-BTC-based metal–organic frameworks, *Chem. Commun.*, 2012, **48**, 8829–8831.
27 T. Panda, T. Kundu and R. Banerjee, Self-assembled one dimensional functionalized metal–organic nanotubes (MONTs) for proton conduction, *Chem. Commun.*, 2012, **48**, 5464–5466.
28 S. Bhattacharya, M. Gnanavel, A. J. Bhattacharyya and S. Natarajan, Organization of Mn-clusters in pcu and bcu networks: synthesis, structure, and properties, *Cryst. Growth Des.*, 2014, **14**, 310–325.
29 B. Hao, X. Wang, C. Zhang and Q. Wang, Two Hydrogen-Bonded Organic Frameworks with Imidazole Encapsulation: Synthesis and Proton Conductivity, *Cryst. Growth Des.*, 2021, **21**, 3908-3915.
30 X. Meng, X. Z. Song, S. Y. Song, G. C. Yang, M. Zhu, Z. M. Hao, S. N. Zhao and H. J. Zhang, A multifunctional proton-conducting and sensing pillar-layer framework based on [24-MC-6] heterometallic crown clusters, *Chem. Commun.*, 2013, **49**, 8483–8485.
31 M. Zhu, Z. M. Hao, X. Z. Song, X. Meng, S. N. Zhao, S. Y. Song and H. J. Zhang, A new type of double-chain based 3D lanthanide(III) metal-organic framework demonstrating proton conduction and tunable emission, *Chem. Commun.*, 2014, **50**, 1912–1914.
32 T. Satoshi, C. François-Xavier and N. Tadaaki, Insulator-to-proton-conductor transition in a dense metal−organic framework, *J. Am. Chem. Soc.,* 2015, **137**, 6428–6431.
33 X. Y. Dong, X. P. Hu, H. C. Yao, S. Q. Zang, H. W. Hou and T. C. Mak, Alkaline earth metal (Mg, Sr, Ba)-organic frameworks based on 2,2',6,6'-tetracarboxy-biphenyl for proton conduction, *Inorg. Chem.*, 2014, **53**, 12050–12057.
34 T. Panda, T. Kundu and R. Banerjee, Structural isomerism leading to variable proton conductivity in indium(III) isophthalic acid based frameworks, *Chem. Commun.*, 2013, **49**, 6197–6199.
35 M. Bazaga-García, M. Papadaki, R. M. P. Colodrero, P. Olivera-Pastor, E. R. Losilla, B. Nieto-Ortega, M. Á. G. Aranda, D. Choquesillo-Lazarte, A. Cabeza and K. D. Demadis, Tuning proton conductivity in alkali metal phosphonocarboxylates by cation size-induced and water-facilitated proton transfer pathways, *Chem. Mater.*, 2015, **27**, 424–435.
36 N. E. Wong, P. Ramaswamy, A. S. Lee, B. S. Gelfand, K. J. Bladek, J. M. Taylor, D. M. Spasyuk and G. K. H. Shimizu, Tuning intrinsic and extrinsic proton conduction in metal–organic frameworks by the lanthanide contraction, *J. Am. Chem. Soc.*, 2017, **139**, 14676–14683.
37 F. M. Zhang, L. Z. Dong, J. S. Qin, W. Guan, J. Liu, S. L. Li, M. Lu, Y. Q. Lan, Z. M. Su and H. C. Zhou, Effect of emidazole arrangements on proton-conductivity in metal–organic frameworks, *J. Am. Chem. Soc.*, 2017, **139**, 6183–6189.
38 S. Pili, S. P. Argent, C. G. Morris, P. Rought, V. Garcia-Sakai, I. P. Silverwood, T.

L. Easun, M. Li, M. R. Warren, C. A. Murray, C. C. Tang, S. Yang and M. Schroder, Proton conduction in a phosphonate-based metal–organic framework mediated by intrinsic "Free Diffusion inside a Sphere", *J. Am. Chem. Soc.*, 2016, **138**, 6352–6355.

39 X. Liang, S. Wang, S. Zhang, C. Lin, F. Xie, R. Li, F. Zhang, C. Wen, L. Feng and C. Wan, High proton conductivity modulated by active protons in 1D ultra-stable metal–organic coordination polymers: a new insight into the coordination interaction/ability of metal ions, *Inorg. Chem. Front.*, 2023, **10**, 1238–1254.

40 X. Liang, F. Zhang, H. Zhao, W. Ye, L. Long and G. Zhu, A proton-conducting lanthanide metal–organic framework integrated with a dielectric anomaly and second-order nonlinear optical effect, *Chem. Commun.*, 2014, **50**, 6513–6516.

41 X. Liang and Z. Fan, Structural characterization and proton-conductive property of a lanthanide metal-organic framework assembled from 1, 2, 4, 5-benzenetetracarboxylic acid and piperazine, *Chin. J. Struct. Chem.*, 2017, **36**, 977–984.

42 X. Liang, K. Cai, F. Zhang, J. Liu and G. Zhu, A proton-conductive lanthanide oxalatophosphonate framework featuring unique chemical stability: stabilities of bulk phase and surface structure, *J. Mater. Chem. A*, 2017, **5**, 25350–25358.

43 X. Liang, K. Cai, F. Zhang, J. Liu and G. Zhu, One, two, and three-dimensional metal–organic coordination polymers derived from enantiopure organic phosphorate: homochirality, water stability and proton conduction, *CrystEngComm*, 2017, **19**, 6325–6332.

44 X. Liang, T. Cao, L. Wang, C. Zheng, Y. Zhao, F. Zhang, C. Wen, L. Feng and C. Wan, From an organic ligand to a metal–organic coordination polymer, and to a metal–organic coordination polymer–cocrystal composite: a continuous promotion of the proton conductivity of crystalline materials, *CrystEngComm*, 2020, **22**, 1414–1424.

45 M. Liu, L. Chen, S. Lewis, S. Y. Chong, M. A. Little, T. Hasell, I. M. Aldous, C. M. Brown, M. W. Smith, C. A. Morrison, L. J. Hardwick and A. I. Cooper, Three-dimensional protonic conductivity in porous organic cage solids, *Nat. Commun.*, 2016, **7**, 12750.

46 X. Liang, T. Cao, L. Wang, C. Zheng, Y. Zhao, F. Zhang, C. Wen, L. Feng and C. Wan, From an organic ligand to a metal–organic coordination polymer, and to a metal–organic coordination polymer–cocrystal composite: a continuous promotion of the proton conductivity of crystalline materials, *CrystEngComm*, 2020, **22**, 1414–1424.

47 A. Garai, A. G. Kumar, S. Banerjee and K. Biradha, Proton-Conducting Hydrogen-Bonded 3D Frameworks of Imidazo-Pyridine-Based Coordination Complexes Containing Naphthalene Disulfonates in Rhomboid Channels, *Chem. Asian J.*, 2019, **14**, 4389–4394.

48 S. Zheng, L. Li, L. Chen, Z. Fan, F. Xiang, Y. Yang, Z. Zhang and S. Xiang, Two Water Stable Phosphate-Amidinium Based Hydrogen-Bonded Organic Framework with Proton Conduction, *Z. Anorg. Allg. Chem.*, 2022, **648**, e202200031.

49 H. Zeng, Y. Tang, L. Luan, X. Dong, G. Zou and Z. Lin, Ionothermal synthesis and

proton conductive behaviors of an organic–inorganic hybrid nickel dihydrogen phosphate, *Inorg. Chem. Commun.*, 2023, **151**, 110559.